Gradients of Be-dopant concentration in self-catalyzed GaAs nanowires

Marcelo Rizzo Piton[1,2], Eero Koivusalo[2], Teemu Hakkarainen[2], Helder Vinicius Avanço Galeti[3], Ariano De Giovanni Rodrigues[1], Soile Talmila[2], Sergio Souto[4], Donald Lupo[5], Yara Galvão Gobato[1,6] and Mircea Guina[2]

[1] *Physics Department, Federal University of São Carlos, São Carlos-SP, Brazil*

[2] *Optoelectronics Research Centre, Physics Unit, Tampere University, Tampere, Finland*

[3] *Electrical Engineering Department, Federal University of São Carlos, São Carlos-SP, Brazil*

[4] *FZEA/ZAB, University of São Paulo, Pirassununga-SP, Brazil*

[5] *Electronics and Communications Engineering, Tampere University, Tampere, Finland*

[6] *High Field Magnetic Laboratory, Radboud University, The Netherlands*

KEYWORDS: Nanowires, GaAs, Be doping, Concentration profiles

Abstract

Effective and controllable doping is instrumental for enabling the use of III-V semiconductor nanowires in practical electronics and optoelectronics applications. To this end, dopants are incorporated during self-catalyzed growth via vapour-liquid-solid mechanism through the catalyst droplet or by vapour-solid mechanism of the sidewall growth. The interplay of these mechanisms together with the competition between axial elongation and radial growth of nanowires can result in dopant concentration gradients along the nanowire axis. Here, we report an investigation of Be-doped p-type GaAs nanowires grown by the self-catalyzed method on lithography-free Si/SiO_x templates. The influence of dopant incorporation on the structural properties of the nanowires is analysed by scanning and transmission electron microscopy. By combining spatially resolved Raman spectroscopy and transport characterization, we are able to estimate the carrier concentration, mobility and resistivity on single nanowire level. We show that Be dopants are incorporated predominantly by vapour-solid mechanism for low Be flux, while the relative contribution of vapour-liquid-solid incorporation is increased for higher Be flux, resulting in axial dopant gradients that depend on the nominal doping level.

1. Introduction

Semiconductor III-V nanowires (NWs) have emerged due to their unique properties and development opportunities they render possible to a wide range of optoelectronics devices [1,2], such as LEDs [3,4], solar cells [5,6], and photodetectors [7]. The one-dimensional NW geometry brings specific advantages including the possibility to combine different semiconductor alloys as radial and axial heterostructures, and relaxes the lattice matching requirements; in turn, this enables III-V semiconductor NW growth on dissimilar substrates such as Si [1] which is widely used in electronics. Going into more details of the fabrication of such NWs, the self-catalyzed growth [8,9] has been adopted for direct epitaxial integration because it avoids the use of foreign catalyst metals such as Au, which is known to form deep traps in Si and therefore degenerate device performance [10]. Substantial progress has been made recently in self-catalyzed growth of GaAs NWs with high control of the size distributions and crystalline

structure [11–16]. Moreover, the ability to achieve an effective and controllable doping is essential for bringing these nanostructures to the realm of practical applications, for example enabling formation of p-n junctions without compromising the material quality of the NWs. It should be emphasized that the knowledge of the dopant incorporation in traditional thin film epitaxy cannot be directly applied to NW growth. Therefore, significant effort has been dedicated to investigate the dopant incorporation mechanisms in NW growth [17]. The dopants are incorporated in NWs either via vapor-liquid-solid (VLS) mechanism through the catalyst droplet, or via vapor-solid (VS) mechanism during the sidewall growth. The incorporation of p-type dopant Be into GaAs NWs during self-catalyzed growth has been investigated by several groups and different incorporation mechanisms have been reported. Casadei et al. reported a preferential VS Be incorporation via the NWs sidewalls [18]. Zhang et al. proposed a predominance of Be incorporation through the Ga catalyst droplets [19] and in the work of Dastjerdi et al. it was determined that Be dopants incorporated through truncated facets under the Ga droplet followed by diffusion into the core of the NWs [20]. These previous studies suggest that the Be incorporation strongly depends on the growth conditions.

Here, we report an investigation of Be-doped self-catalyzed GaAs NWs grown on lithography-free Si/SiO_x templates fabricated by droplet epitaxy and spontaneous oxidation of Si substrates [11,12]. We examine the microstructural changes caused by Be dopant incorporation and, in particular, assess the dopant concentration and its axial variations by single-NW Raman and electrical characterization techniques, respectively. We show that different axial gradients of Be concentration are formed for different Be fluxes. Our results suggest that the predominant Be incorporation mechanism is VLS for high Be flux and VS for low Be flux.

2. Experimental Methods

The self-catalyzed GaAs NWs were grown by solid-source molecular beam epitaxy (MBE) on lithography-free oxide patterns fabricated on p-Si(111) substrates by droplet epitaxy and spontaneous oxidation. GaAs droplet epitaxy was performed on oxide-free HF-etched substrates. After the droplet epitaxy, the wafers were removed from the MBE reactor, oxidized in air and loaded back to the MBE.

Prior to NW growth, the samples were annealed for 30 min at 655 °C, as determined by pyrometer, in order to evaporate the GaAs mounds and to reveal oxide-free holes for NW nucleation as described in detail in Ref. [12]. The nucleation site density of the templates used was 2×10^{8} cm^{-2}. The annealing was followed by a 60 s Ga pre-deposition at the NW growth temperature of 640 °C with Ga flux corresponding to planar 0.3 μm/h growth rate on GaAs(100). The NW growth was then initiated by providing As_2 corresponding to a V/III beam equivalent pressure ratio (BEP) of 9. The NWs were grown for 60 min and the growth was terminated by switching off all fluxes simultaneously and rapidly cooling down the sample. The NWs were doped with Be fluxes corresponding to a nominal p-type dopant concentrations of 2.0×10^{18} cm^{-3} and 2.0×10^{19} cm^{-3} for samples hereafter named Be1 and Be2, respectively. The doping levels were calibrated based on Hall measurements of three planar Be-doped GaAs(100) samples grown on semi-insulating GaAs substrates. The thin film (TF) samples were later used for comparing the carrier concentration and mobility values obtained from Raman spectroscopy and Hall measurements, and will be from now on named TF1, TF2 and TF3, in the order of increasing Be flux used during the growth.

The structural properties of NWs were characterized by scanning electron microscopy (SEM) and transmission electron microscopy (TEM). SEM characterization was performed to collect dimensional data and to obtain images of the NWs used for Raman spectroscopy and transport characterization after the measurements were carried out. TEM was used to analyze the microstructure of single NWs harvested from the as-grown samples to a carbon film of a Cu TEM grid; for the analyses we used a FEI Tecnai G2-F20 operating at 200 kV.

Room temperature Raman spectra of single NWs were obtained on backscattering geometry. The NWs were transferred to a Si substrate with a 200 nm SiO_2 thermal oxide layer. The excitation wavelength was 532 nm and a 50x magnification lens with NA=0.82 was used to obtain a spot size of <1 μm in diameter. Raman spectra with varying excitation power were first collected from test NWs to select the optimal power density that would not result in any shifts or broadening of Raman peaks due to laser-induced heating. The linear polarization of both excitation laser and scattered light were adjusted perpendicular to the NW growth axis. The TF samples were also investigated by Raman

spectroscopy with equivalent configuration of linear polarizations of excitation and detection to evaluate the methodology adopted on analysis of the Raman spectra for assessing the free carrier concentration and mobility.

For single-NW transport characterization, the NWs were first drop-casted on a p-GaAs substrate covered by a 200 nm SiO_2 layer with pre-patterned gold pads. The position of representative NWs on the substrate were identified by SEM imaging and electron beam lithography was used to fabricate electrical contacts on individual NWs. After resist development, the sample was dipped in 1:10 $HCl:H_2O$ solution for 10 s to remove the native oxide, followed by 15% ammonium polysulfide $(NH_4)2S_x$ diluted in H_2O for chemical passivation (45 °C, 3 min) of the exposed contact area of the NWs. After chemical treatments of the surface, the NWs were immediately taken to an electron beam metal evaporation equipment and a Pt/Ti/Pt/Au (5/10/10/200 nm) metallic multilayer was deposited on the sample. After lift-off of the resist, a rapid thermal annealing at 400 °C for 30 s was performed to reduce the contacts resistance. Current-voltage (IV) measurements were carried using an Agilent Source-Meter Unit.

3. Results and discussion

3.1 Structural properties

TEM and HR-TEM images from selected areas of undoped and Be-doped GaAs NWs were obtained to evaluate the influence of Be incorporation on the microstructural properties of the NWs. The results are summarized in figures. 1(a)-(d) for undoped NWs, in figures 1(e)-(h) for Be1 NWs, and in figures 1(i)-(l) for Be2 NWs. The bright-field (BF) TEM image of undoped NW in figure 1(a) shows that the twin plane density increases towards the NW/droplet interface, region at which the contact angle between the Ga droplet and NW tip decreases due to lateral growth favoring the twin plane formation [12]. HR-TEM imaging of the root region in figure 1(d) shows a 100 nm long section of stacking faults and polytypism, followed by a 2 μm long center region of pure zincblend (ZB) GaAs, as shown in figure 1(c). A short wurtzite (WZ) section (~5 nm) was formed at the interface of the Ga droplet and the NW body (figure 1(b)), which is commonly observed in self-catalyzed growth of GaAs NWs due to rapid

changes in the growth conditions after switching off the Ga and As fluxes and subsequent ramp down of the sample temperature [12].

The BF images of Be1 and Be2 NWs are shown figures 1(e) and 1(i), respectively. The twin plane density at the center-tip regions is smaller than in the undoped sample shown in figure 1(a), which has been previously reported for self-catalyzed Be-doped GaAs NWs [19]. The root regions of Be1 and Be2 NWs, shown in figures 1(h) and 1(l), are composed of ZB structure with twin planes and stacking faults due to instabilities related to early-stages of the epitaxial growth, such as Ga droplet composition. It is evident that the incorporation of Be suppresses the twin plane formation in the center [figures 1(g) 1(k)] and NW-droplet interface [figures 1(f) and 1(j)] regions when compared to the undoped sample. The formation of twin planes and WZ segments in self-catalyzed GaAs NWs is commonly attributed to the droplet contact angle [9,21,22]. However, the post growth analysis of the distributions of droplet contact angles reveals no significant difference between the Be doped and undoped NWs (See Fig. S1 in the Supplementary Data). The mean values of contact angles and the standard deviations for Be1, Be2, and undoped NWs are 123.5° ± 4.6°, 126.4° ± 6.2° and 127.8° ± 5.3°, respectively. Furthermore, Be has been reported to suppresses the formation of WZ segments during Ga droplet crystallization [23], which is another indication that the influence of Be on the ZB crystal phase purity cannot be explained merely by a change of droplet contact angle. Therefore, the reduction of twinning and WZ stacking probability in the Be-doped NWs is most likely related to a more complex change of energetics in the VLS system, leading to an increase of ZB nucleation probability over WZ stacking and twin formation. Furthermore, the NWs grown with high Be flux [Be2 in figure 1(k)] exhibit roughening of the (110) sidewall planes along the whole NW length. The selected area electron diffraction (SAED) patterns corresponding to the HR-TEM images of the bottom, center and tip regions of undoped, Be1 and Be2 NWs can be found in figure S2 in the Supplementary Data.

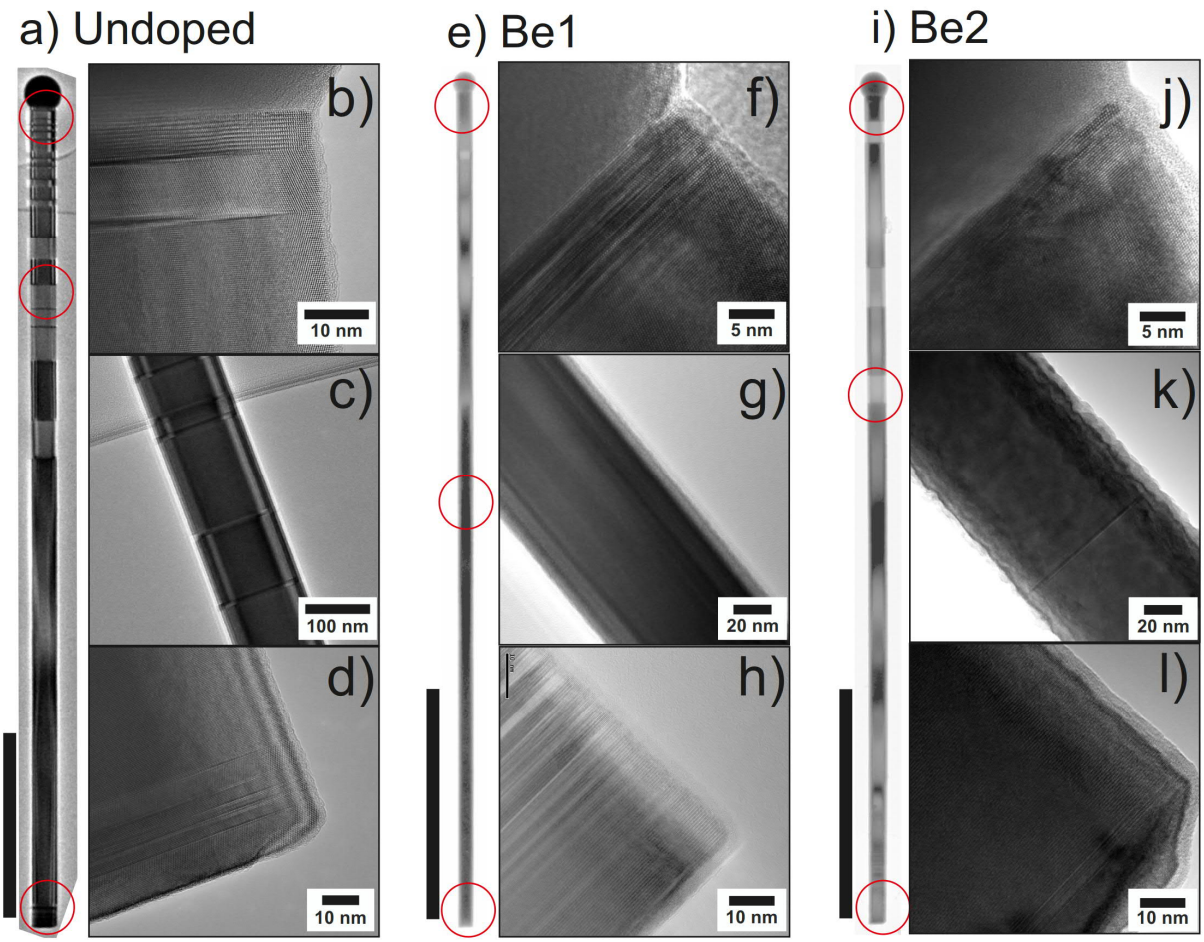

Figure 1. HR-TEM images of (a)-(d) undoped, (e)-(h) Be1, and (i)-(l) Be2 NWs. The red circles in (a), (e) and (i) indicate the different positions corresponding to the higher magnification images in (b)-(d), (f)-(h) and (j)-(l). The scale bars are 1 μm in (a), (e) and (i). The other scale bars sizes are indicated on each figure.

3.2 Raman spectroscopy

Single-NW Raman spectroscopy with microscopic resolution allows to investigate the effect of Be doping in different regions of the NW. Figure 2 shows Raman spectra of undoped, and two samples of Be-doped NWs (namely Be1 and Be2) collected from three different positions along the NW axes. The decomposition of the experimental data in Lorentzian peaks of undoped NWs in figure 2(a) reveals the transversal optical (TO), the surface optical (SO) and the longitudinal optical (LO) vibration modes of ZB GaAs centered at 268, 272 and 288 cm^{-1}, respectively. The SO modes are commonly observed in nanostructures with high surface-to-volume ratio. Its frequency depends on the surrounding medium [24] and density of defects, such as twin planes [25]. It was also reported that doping does not affect

SO mode frequency and linewidth [25]. It is worth mentioning that LO is a forbidden mode in Raman backscattering from (110) surface of ZB crystals [26], but this selection rule is relaxed to some extent for NWs due to finite size effects and hexagonal geometry of the cross section [24]. This allows to analyze the screening of the LO mode due to the presence of free carriers caused by Be incorporation on the NWs lattice [27].

In doped polar semiconductors, such as GaAs, the LO mode can couple to collective oscillations of free carriers producing a coupled-phonon-plasmon mode (CPPM) [28]. The line shape analysis of the CPPM can be used to estimate the free carriers concentrations and holes mobility for p-type GaAs epilayers [28,29] and NWs [18,27,30,31]. The Raman scattering intensity of the CPPM can be described by [32]:

$$I(\omega) = A\omega\Gamma_p\omega_p[\omega_{TO}^2(1+C) - \omega^2]^2/D \quad (1)$$

With:

$$D = \left[\omega^2(\omega_{LO}^2 - \omega^2) - \omega_p^2(\omega_{TO}^2 - \omega^2) + \gamma\Gamma_p\omega^2\right]^2 + \left[\Gamma_p\omega(\omega_{LO}^2 - \omega^2) + \gamma\omega\left(\omega_p^2 - \omega^2\right)\right]^2 \quad (2)$$

In this formulation, ω_{TO} and ω_{LO} are the TO and LO wavenumbers of an undoped reference sample respectively, A is a frequency independent parameter, C = -0.49 is the Faust-Henry coefficient for GaAs at room temperature for 532 nm laser excitation [33] and γ is the natural LO mode damping constant. The hole mobility μ_p can be calculated from the plasmon-damping constant $\Gamma_p = e/\mu_p m_p^*$ and the free carrier concentration p is obtained from the plasma oscillation frequency of the free carriers $\omega_p^2 = pe^2/\epsilon_0\epsilon_\infty m_p^*$. The remaining symbols have the usual meanings: e is the elementary electron charge, m_p* is the hole effective mass, ε_∞ is the high-frequency dielectric constant for GaAs and ε_0 is the vacuum permittivity.

Figures 2(b) and 2(c) show Raman spectra measured at three different positions of representative Be1 and Be2 NWs respectively. The figures include the spectral components related to TO, SO and CPPM modes that best fit the experimental data. On the right side are the corresponding SEM images

indicating the region of the NW from where Raman spectra were measured. The TO peak positions and linewidths are consistent with the undoped sample and the SO position is in accordance to the NW diameters and stacking faults/twin plane densities [24,25] observed in the HR-TEM images. The spectral position and linewidth of the CPPM mode is dependent on the carrier concentration and mobility [28]. The Raman peak at 256 cm^{-1} observed at the root section (P1) of Be2 NW in figure 2(c) corresponds to E_2^H TO mode of WZ phase of GaAs [34] which is consistent with the results from the HR-TEM in figure 1(l).

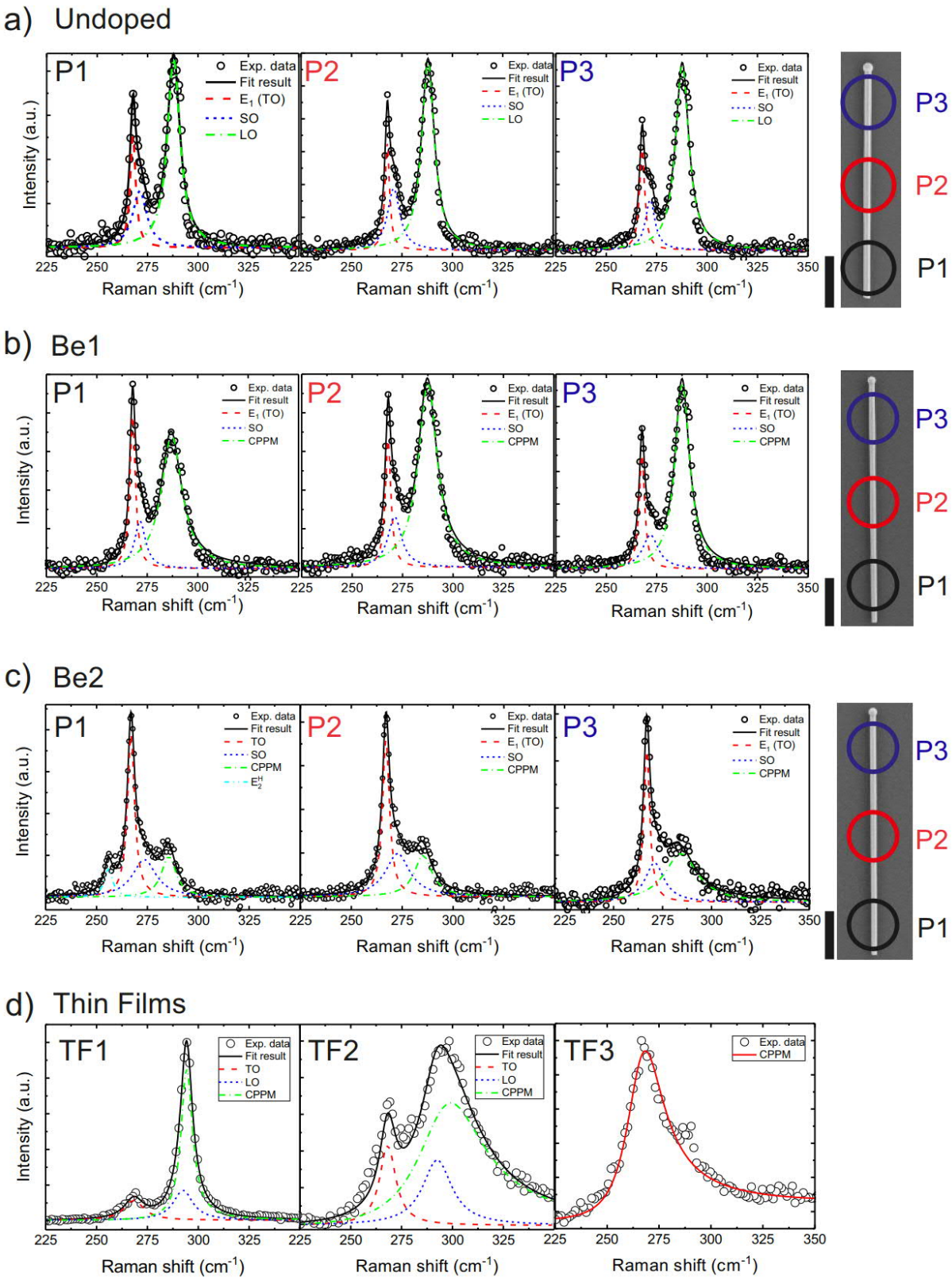

Figure 2. Raman spectra of (a) undoped, (b) Be1, (c) Be2 GaAs NWs, and (d) Be-doped GaAs TF samples. The spectra P1, P2, and P3 were collected from the regions indicated in the SEM pictures of the right sides of (a)-(c). The scale bars in the SEM pictures are 1 μm.

In order to evaluate the fit method applied to the Be1 and Be2 NWs, we analyzed the Raman spectra of TF samples considering the contribution of CPPM calculated through Eq. (1) and comparing the results with the Hall Effect data. The results are summarized in figure 3 for the carrier concentration (figure 3(a)) and the hole mobility (figure 3(b)). The carrier concentrations obtained from Raman and Hall Effect experiments in figure 3(a) are in good agreement, whereas the hole mobilities in figure 3(b) are clearly underestimated by Raman spectroscopy when compared with the Hall effect data. Similar results were previously reported for Zn-implanted GaAs [28] and p-type GaP [35]. In Ref. [35] the differences between values of hole mobility estimated by Raman and Hall effect are attributed to the contributions of several other factors that may cause an apparent decrease in the hole mobility at room temperature estimated by Raman spectroscopy, such as non-polar optical and acoustic phonons, polar optical phonons and ionized impurities [35,36].

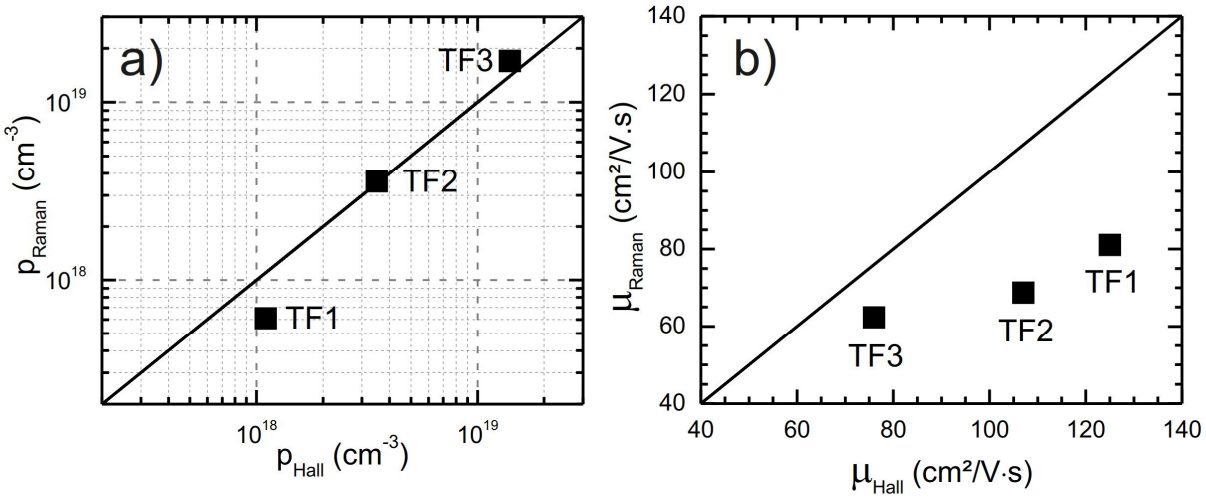

Figure 3. (a) Carrier concentration and (b) Hole mobility comparison between Hall effect data and fit of CPPM peak from Raman spectra of TF samples. The symbols represent the fit results and the solid lines, indicating one-to-one relation between Hall and Raman values, are for illustrational purposes.

By applying the same fitting procedure to the spectra in figures 2(b) and 2(c), we calculated the charge carrier concentrations and the hole mobilities of three representative NWs of each nominal doping level. The results of carrier concentration and hole mobility are presented in figures 4(a) and 4(b), respectively. The Raman spectra of the additional NWs from Be1 and Be2 samples are included in figure S3 in the Supplementary Data. The dashed lines in figure 4(a) represent the nominal doping

level of Be1 and Be2 samples. The hole concentrations from the NWs in figure 4(a) ranges from 8×10^{17} to 1.6×10^{18} cm^{-3} for Be1 NWs (nominal 2×10^{18} cm^{-3}) and from 3.4×10^{18} to 1.1×10^{19} cm^{-3} for Be2 NWs (nominal 2×10^{19} cm^{-3}). There is no consistent spatial dependence of Be concentration that would suggest a doping profile along the NW axis, but the variation of values obtained for different axial positions are rather large for all investigated NWs. Some uncertainty of the fitting results is expected due to overlapping of TO, SO and CPPM. As the dopant concentration increases, the CPPM mode gets broader and shifts to frequencies closer to the TO mode of ZB GaAs [28], which increases the uncertainty of the line shape analysis in which Eq. (1) is used as a component for spectral decomposition. Nevertheless, the fitting results were consistent with the same methodology applied to the thin film samples supported by Hall Effect measurements in figure 3.

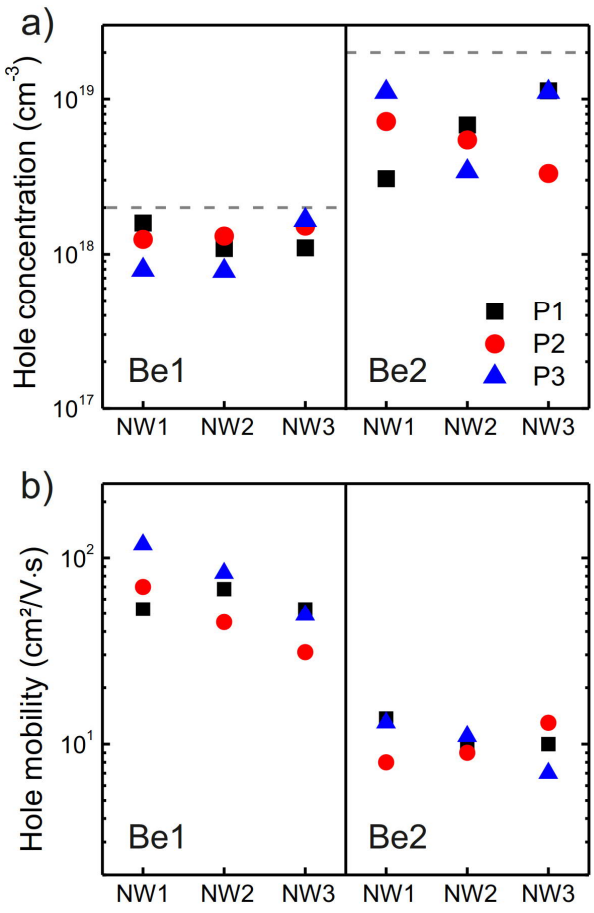

Figure 4. (a) Hole concentration and (b) hole mobility, obtained from the fit of CPPM lineshape to the Raman spectra for three different NWs extracted from Be1 and Be2 samples. The NW1 data points in (a) and (b) corresponds to the spectra presented in figures 2(b) and (c), respectively. The spectra corresponding to the NW2

and NW3 data points are shown in figure S3. The symbols represent the different positions of the NWs from which the Raman spectrum was measured: bottom region (P1), center region (P2) and tip region (P3). The grey dashed lines (a) represent the nominal Be concentration of each sample.

The carrier concentrations of Be1 and Be2 NWs are shown in figure 4(a) and are compared with the nominal dopant concentrations, which are indicated by the dashed grey lines. On average, the carrier concentration of Be1 NW is 60% from the nominal doping whereas Be2 NW present 35% of the nominal doping level. Similar incorporation efficiency of Be dopant in self-catalyzed GaAs NWs has been reported [30]. It is important to highlight that the Be fluxes used for nominal doping of the NWs are based on Hall Effect data obtained from the (100) oriented GaAs epilayers and the Be incorporation rates are expected to be different for VS incorporation at the (110) oriented NW sidewalls and for the VLS mechanism through the droplet [18–20]. Moreover, the results from Be1 and Be2 NWs suggest a reduction of the incorporation efficiency at higher Be flux. On the other hand, the hole mobilities [figure 4(b)] obtained for Be1 NW are similar to the values from Raman spectroscopy of the TF samples having similar carrier concentration. However, the values obtained for the mobility of Be2 NWs were significantly lower than what is expected for similar dopant concentration of bulk Be-doped GaAs at room temperature. Similar result was also observed in Be-doped GaAs NWs and ascribed to scattering at the surface [27] that would considerably decrease the mean free path of the carriers. It should be noted that the charge carriers in highly doped NWs are expected to be more affected by the surface due to the small depletion layer width [18].

3.3 Transport properties

The spatial dependence of the transport properties of individual Be-doped NWs was investigated by manufacturing evenly spaced contacts and analyzing the IV characteristics of each channel along the NWs. Figure 5(a) shows representative IV curves from Be1 sample and the corresponding SEM image of the device in figure 5(b). The asymmetric IV indicate a Schottky-like behavior of the metal-semiconductor contacts. The current values in different positions along the Be1 NW in figure 5(a) indicate an increase in the values of the Schottky barrier heights in the contacts from the bottom (AB

channel) to tip (CD channel) of the NW. This behavior can be associated to a dopant concentration profile which decreases from the root toward the tip of the NW. Such behavior was observed consistently for all investigated Be1 NWs, as shown in figures S4(a) and S4(e) in the Supplementary Data. It should be noted that most of the Ga droplets were removed in the contact fabrication process, unlike in the case of the NW shown in figure 5. In those cases, the bottom end of the NW was identified from the specific off-cut shape formed when the NWs were harvested from the substrate. The insets in figure 5(b) show higher magnification SEM pictures of the bottom (contact A) end with the off-cut shape and tip end (contact D) of the NW. More details can be found in figures S4, S5 and S6 in the Supplementary Data.

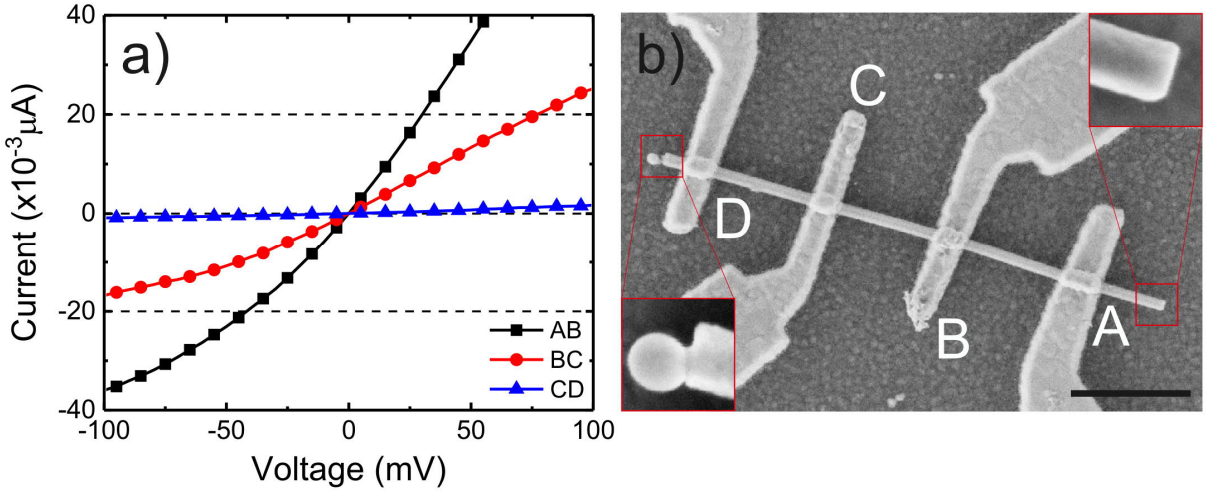

Figure 5. (a) IV characteristics of different channels along Be1 NW. (b) An SEM image of measured device. Each channel in (a) corresponds to a pair of contacts as indicated in (b), with A being at the bottom and D at the tip region of the NW. The scale bar in (b) is 1 µm. The insets in (b) show higher magnification SEM pictures of the bottom (contact A) and tip (contact D) of the NW.

Figure 6 shows similar IV curves for Be2 NWs. In contrast to Be1, the IV curves are linear and exhibit smaller differences in the current values between different channels. This also confirms that the surface passivation by ammonium polysulfide and the choice of the metal layers used for device processing were successful in achieving ohmic contacts to p-GaAs NWs. The bottom (channel AB) and tip (channel CD) parts of the NW without the Ga droplet in figure 6(b) were identified by the same method previously described. The insets in figure 6(b) show higher magnification SEM pictures of the

bottom (contact A) end with the off-cut shape and tip end (contact D) of the NW. The slope in the IV curve depends on both contact resistance and semiconductor resistivity. Therefore, in the following we present another transport experiment for distinguishing these two values.

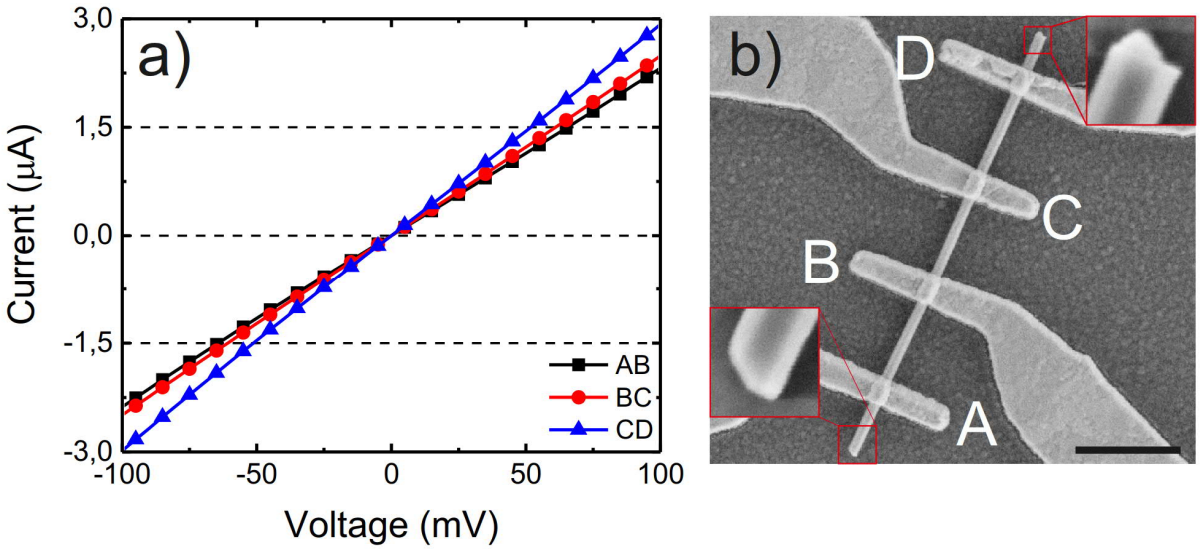

Figure 6. a) IV characteristics of different channels along Be2 NW. (b) SEM image of measured device. Each channel in (a) corresponds to a pair of contacts as indicated in (b), with A being at the bottom and D at the tip region of the NW. The scale bar in (b) is 1 μm. The insets in (b) show higher magnification SEM pictures of the bottom (contact A) and tip (contact D) of the NW.

The ohmic character of the IVs from Be2 NWs allowed us to estimate simultaneously the contact specific resistance and the semiconductor resistivity by fabricating five electrical contacts with increasing channel length along the NW axial direction, also known as transmission line model (TLM) geometry [37]. In this configuration, the total resistance R_T of each channel was obtained from the slope of the IV curves and plotted as a function of channel length, the NW resistivity ρ_s and transfer length L_T were then obtained by fitting the pairs (R_T, L) using the relation [37,38]:

$$R_T(L) = \frac{\rho_s}{\pi r^2}\left(2L_T \coth\left(\frac{W_C}{L_T}\right) + L\right) \quad (3)$$

Where W_C is the contact width and r is the NW radius obtained by SEM imaging of the devices after transport measurements. This equation format was chosen over a linear fit of the experimental points to

account for the reduced contacts width used in our devices due to NW length limitations [37]. The specific contact resistance ρ_c can be obtained from the equation:

$$\rho_c = \frac{3}{2}\frac{\rho_s}{r}L_T^2 \quad (4)$$

Where the pre-factor 3/2 accounts for the fact the metal contact layer is not covering the whole NW surface [37]. The specific contact resistance obtained from TLM devices allowed us to calculate the nanowire resistivity of the devices similar to presented in figure 6(a) by using equation (5):

$$R_T = \rho_S\frac{L}{A} + 2R_C \quad (5)$$

Where A is the hexagonal cross-section area of the NW.

Figure 7(a) shows the IV of different channel lengths of Be2 NW in the TLM geometry, the inset shows the SEM picture of the device obtained after transport measurements. The total resistance of the longer channel (L = 1.10 μm) was unexpectedly smaller than the shorter center channels most likely as a result of the contact overlap with one of the ends of the NW, resulting in smaller contact resistance. Therefore, this data point is omitted from the fitting procedure. The fitting to the experimental data in figure 6(b) resulted in nanowire resistivity of ρ_S=0.027 Ω·cm and specific contact resistance of ρ_C=4.5x10^{-6} Ω·cm², the transfer length resulting from the best-fit values was L_T = 230 nm. Based on the values of ρ_C obtained, the total contact resistance for each channel is 18 kΩ on average. Comparable results of contact resistance were previously reported for Zn-implanted p-type GaAs NWs with similar metal contact multilayer [39] and Be-doped GaAs thin films [40].

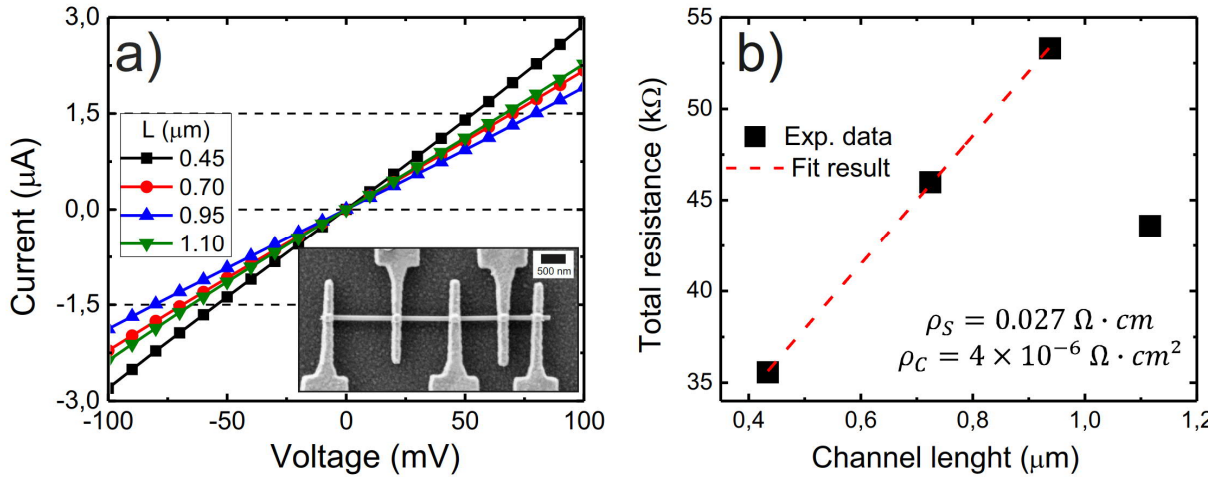

Figure 7. (a) IV characteristics of Be2 NW measured in TLM geometry. The inset shows an SEM image of the measured device. The scale bar is 500 nm. (b) Total resistances of individual channels as a function of channel length. The square points are obtained from the linear fit to the IV curves in (a) and the red dashed line is the fit result using equation (3).

With the specific contact resistance value now determined, we are able to calculate the semiconductor resistivity for each channel of the evenly spaced contacts shown in figure 6 (NW1) and other NWs from the same sample (NW2 and NW3, figure S5 of Supplementary Data) using equation (6). The NW diameters were measured by SEM images obtained after transport measurements and a hexagonal cross-section area was considered. Figure 8 shows the resistivity from channels AB (bottom region), BC (center region) and CD (tip region) of NW1, NW2 and NW3. The NW resistivity obtained from TLM is represented by the dashed line for comparison. The resistivity values range from 0.023 Ω·cm to 0.033 Ω·cm. It should be noted that the TLM calculations are based on nanowires with circular cross-sections [37] whereas the resistivity was calculated assuming more realistic hexagonal cross section for the devices with evenly spaced contacts. This explains slight deviation of the resistivity values obtained from the two methods, as can be seen from figure 8. Nevertheless, the resistivity calculated for the evenly spaced contacts allows us to investigate the Be concentration gradient in the axial direction for Be2 NWs. While there is some NW-to-NW variation in the resistivity values, we consistently observe lower resistivity for the upper part than for the lower part of the NW, indicating axial Be concentration gradient which increases towards the tip, which is contrary to what was observed for Be1.

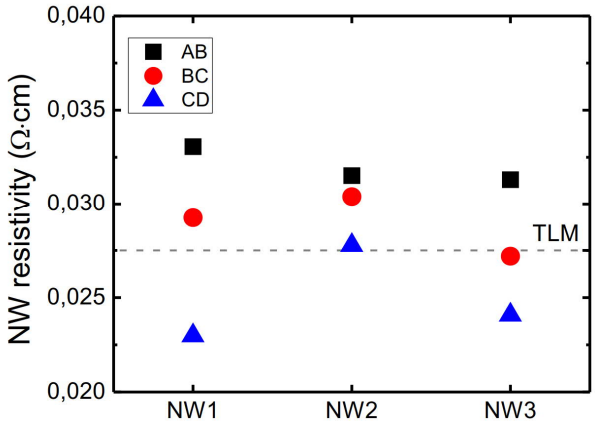

Figure 8. Nanowire resistivity of Be2 NWs from devices similar to presented in figure 6(a). The experimental points were calculated using equation (5) for each channel along the NW length, with A being at the bottom and D at the tip region of the NW. The dashed line indicates the NW resistivity value obtained by TLM.

From the IV analysis of the NW devices in figures 5(a), 6(a) and 8 it is clear that the Be dopant gradient is opposite in Be1 and Be2 samples grown with lower and higher Be flux, respectively. The IV data of Be1 indicates a dopant gradient with decreasing concentration from bottom to tip. The thickness of the VS grown shell is larger at the bottom than at the tip region of the NW, as the NWs grow constantly in thickness but are not tapered [13,41]. Thus, in sample Be1, the Be dopants incorporate predominantly through the NW sidewalls via VS growth, as reported in [18]. Predominant Be incorporation via VLS mechanism through the Ga droplet would result in a dopant gradient which increases from bottom to tip [19,20], as the thickness of the VLS grown core increases from bottom to tip [41]. This is indeed what we observe for Be2. Therefore, we conclude that the predominant dopant incorporation pathway depends on the Be flux so that lower Be fluxes favorably incorporate via VS growth and higher fluxes via VLS growth. In case of the lower Be flux, the VLS incorporation can be limited by capture of Be atoms only by direct impingement to the Ga droplet, while the axial VLS growth rate is more than 10-times larger than the nominal growth rate of 0.3 µm/h for which the nominal doping level is calibrated, thus leading the predominant VS incorporation. As for the high Be flux, it should be noted that, according to the Raman results shown in figure 4(a), the total incorporation efficiency decreases when the Be flux is increased. Therefore, the difference between the dopant gradients of Be1 and Be2 NWs is more likely due to a reduction of the VS incorporation than an increase

of the VLS incorporation when the Be flux is increased. Such saturation of the VS incorporation can be attributed to the onset of Be segregation on the GaAs surface. In the planar VS growth of Be-doped GaAs, the segregation at high Be fluxes causes an increase of surface roughness [42–44], which is indeed observed in figure 1(k) in the TEM micrographs of the NWs grown with high Be flux. When planar layers are grown by VS with typical 1 μm/h growth rates, the segregation effects are expected at high doping levels in the 10^{19}-10^{20} cm^{-3} range. However, the radial growth rate on the NW sidewalls by the VS mechanism is significantly lower and, according to the thermodynamic model presented in Ref. [43], low growth rates lead to an onset of segregation at lower doping levels. The same model also predicts that the onset of Be segregation depends on the As flux and growth temperature, which further emphasizes the influence of growth conditions on the Be incorporation in self-catalyzed GaAs NW growth.

4. Conclusions

We have investigated the effect of Be-dopant incorporation in self-catalyzed GaAs NWs using a lithography-free fabrication technique of Si/SiO_x templates. The presence of Be impurities was found to suppress the formation of twin planes and stacking faults in the NWs. Using spatially resolved single-NW Raman spectroscopy and transport characterization, we were able to assess the dopant incorporation and axial dopant gradients formed in NWs grown with higher and lower Be fluxes. We have shown that with low Be flux the dopant concentration decreases towards the NW tip, while for high Be flux the gradient is opposite. These results suggest that the Be dopants incorporate predominantly via VS growth at the NW sidewalls with low Be flux, while the relative contribution of the VLS mechanism becomes more significant when the Be flux is increased.

Acknowledgements

M.R.P. acknowledges CAPES/CNPq process 88887.100549/2015-00, H.V.A.G. and Y.G.G. acknowledge FAPESP grants 18/01808-5, 16/10668-7 and 14/50513-7. M.R.P, E.K, T.H, and M.G. acknowledge financial support from the Academy of Finland Project NESP (decision number 294630), and NanoLight (decision number 310985) and the Vilho, Yrjö and Kalle Väisälä Foundation of the

Finnish Academy of Science and Letters. This work made use of Tampere Microscopy Center facilities at Tampere University.

References

[1] Joyce H J et al 2011 III–V semiconductor nanowires for optoelectronic device applications *Prog. Quantum Electron.* **35** 23–75

[2] Zhang A, Zheng G and M. Lieber C 2016 *Nanowires: Building Blocks for Nanoscience and Nanotechnology* (New York: Springer International Publishing)

[3] Dimakis E et al 2014 Coaxial Multishell (In,Ga)As/GaAs Nanowires for Near-Infrared Emission on Si Substrates *Nano Lett.* **14** 2604–9

[4] Svensson C P T, Mårtensson T, Trägårdh J, Larsson C, Rask M, Hessman D, Samuelson L and Ohlsson J 2008 Monolithic GaAs/InGaP nanowire light emitting diodes on silicon *Nanotechnology* **19** 305201

[5] Aberg I et al 2016 A GaAs Nanowire Array Solar Cell With 15.3% Efficiency at 1 Sun *IEEE J. Photovoltaics* **6** 185–90

[6] van Dam D, van Hoof N J J, Cui Y, van Veldhoven P J, Bakkers E P A M, Gómez Rivas J and Haverkort J E M 2016 High-Efficiency Nanowire Solar Cells with Omnidirectionally Enhanced Absorption Due to Self-Aligned Indium–Tin–Oxide Mie Scatterers *ACS Nano* **10** 11414–9

[7] Thompson M D et al 2016 Low Leakage-Current InAsSb Nanowire Photodetectors on Silicon *Nano Lett.* **16** 182–7

[8] Colombo C, Spirkoska D, Frimmer M, Abstreiter G and Fontcuberta i Morral A 2008 Ga-assisted catalyst-free growth mechanism of GaAs nanowires by molecular beam epitaxy *Phys. Rev. B* **77** 155326

[9] Cirlin G E et al 2010 Self-catalyzed, pure zincblende GaAs nanowires grown on Si(111) by

molecular beam epitaxy *Phys. Rev. B* **82** 035302

[10] Bullis W M 1966 Properties of gold in silicon *Solid. State. Electron.* **9** 143–68

[11] Hakkarainen T V., Schramm A, Mäkelä J, Laukkanen P and Guina M 2015 Lithography-free oxide patterns as templates for self-catalyzed growth of highly uniform GaAs nanowires on Si(111) *Nanotechnology* **26** 275301

[12] Koivusalo E, Hakkarainen T and Guina M 2017 Structural Investigation of Uniform Ensembles of Self-Catalyzed GaAs Nanowires Fabricated by a Lithography-Free Technique *Nanoscale Res. Lett.* **12** 192

[13] Koivusalo E S, Hakkarainen T V., Guina M D and Dubrovskii V G 2017 Sub-Poissonian Narrowing of Length Distributions Realized in Ga-Catalyzed GaAs Nanowires *Nano Lett.* **17** 5350–5

[14] Tauchnitz T, Nurmamytov T, Hübner R, Engler M, Facsko S, Schneider H, Helm M and Dimakis E 2017 Decoupling the Two Roles of Ga Droplets in the Self-Catalyzed Growth of GaAs Nanowires on SiO x /Si(111) Substrates *Cryst. Growth Des.* **17** 5276–82

[15] Tan S L, Genuist Y, den Hertog M I, Bellet-Amalric E, Mariette H and Pelekanos N T 2017 Highly uniform zinc blende GaAs nanowires on Si(111) using a controlled chemical oxide template *Nanotechnology* **28** 255602

[16] Küpers H, Bastiman F, Luna E, Somaschini C and Geelhaar L 2017 Ga predeposition for the Ga-assisted growth of GaAs nanowire ensembles with low number density and homogeneous length *J. Cryst. Growth* **459** 43–9

[17] Dayeh S A, Chen R, Ro Y G and Sim J 2017 Progress in doping semiconductor nanowires during growth *Mater. Sci. Semicond. Process.* **62** 135–55

[18] Casadei A et al 2013 Doping incorporation paths in catalyst-free Be-doped GaAs nanowires

Appl. Phys. Lett. **102** 013117

[19] Zhang Y et al 2018 Doping of Self-Catalyzed Nanowires under the Influence of Droplets *Nano Lett.* **18** 81–7

[20] Dastjerdi M H T, Fiordaliso E M, Leshchenko E D, Akhtari-Zavareh A, Kasama T, Aagesen M, Dubrovskii V G and LaPierre R R 2017 Three-fold Symmetric Doping Mechanism in GaAs Nanowires *Nano Lett.* **17** 5875–82

[21] Krogstrup P, Curiotto S, Johnson E, Aagesen M, Nygård J and Chatain D 2011 Impact of the liquid phase shape on the structure of III-V nanowires *Phys. Rev. Lett.* **106** 1–4

[22] Jacobsson D, Panciera F, Tersoff J, Reuter M C, Lehmann S, Hofmann S, Dick K A and Ross F M 2016 Interface dynamics and crystal phase switching in GaAs nanowires *Nature* **531** 317–22

[23] Zhang Y et al 2017 Growth of pure zinc-blende GaAs(P) core-shell nanowires with highly regular morphology *Nano Lett.* **17** 4946–50

[24] Spirkoska D, Abstreiter G and Fontcuberta i Morral A 2008 Size and environment dependence of surface phonon modes of gallium arsenide nanowires as measured by Raman spectroscopy *Nanotechnology* **19** 435704

[25] Venkatesan S, Mancabelli T, Krogstrup P, Hartschuh A, Dehm G and Scheu C 2017 Surface optical phonon propagation in defect modulated nanowires *J. Appl. Phys.* **121** 085702

[26] Steele J A, Puech P and Lewis R A 2016 Polarized Raman backscattering selection rules for (hhl)-oriented diamond- and zincblende-type crystals *J. Appl. Phys.* **120** 055701

[27] Ketterer B, Uccelli E and Fontcuberta i Morral A 2012 Mobility and carrier density in p-type GaAs nanowires measured by transmission Raman spectroscopy *Nanoscale* **4** 1789

[28] Irmer G, Wenzel M and Monecke J 1997 Light scattering by a multicomponent plasma coupled

with longitudinal-optical phonons: Raman spectra of p-type GaAs:Zn *Phys. Rev. B* **56** 9524–38

[29] Mlayah A, Carles R, Landa G, Bedel E and Muñoz-Yagüe A 1991 Raman study of longitudinal optical phonon-plasmon coupling and disorder effects in heavily Be-doped GaAs *J. Appl. Phys.* **69** 4064–70

[30] Goktas N I, Fiordaliso E M and LaPierre R R 2018 Doping assessment in GaAs nanowires *Nanotechnology* **29** 234001

[31] Amaduzzi F et al 2016 Tuning the response of non-allowed Raman modes in GaAs nanowires *J. Phys. D. Appl. Phys.* **49** 095103

[32] Mlayah A, Carles R, Landa G, Bedel E and Muñoz-Yagüe A 1991 Raman study of longitudinal optical phonon-plasmon coupling and disorder effects in heavily Be-doped GaAs *J. Appl. Phys.* **69** 4064–70

[33] Zekeng S, Prevot B and Schwab C 1988 Raman Determination of the Faust-Henry Coefficient of GaAs in the 1.9 to 2.7 eV Range at Ordinary and Low Temperatures *Phys. status solidi* **150** 65–72

[34] Zardo I, Conesa-Boj S, Peiro F, Morante J R, Arbiol J, Uccelli E, Abstreiter G and Fontcuberta i Morral A 2009 Raman spectroscopy of wurtzite and zinc-blende GaAs nanowires: Polarization dependence, selection rules, and strain effects *Phys. Rev. B* **80** 245324

[35] Irmer G et al 1991 Determination of the hole concentration and mobility of p-GaP by hall and by raman measurements *Semicond. Sci. Technol.* **6** 1072–8

[36] Wenzel M, Irmer G, Monecke J and Siegel W 1997 Hole mobilities and the effective Hall factor in p-type GaAs *J. Appl. Phys.* **81** 7810–6

[37] Mohney S E, Wang Y, Cabassi M A, Lew K K, Dey S, Redwing J M and Mayer T S 2005 Measuring the specific contact resistance of contacts to semiconductor nanowires *Solid. State.*

Electron. **49** 227–32

[38] Park H, Beresford R, Hong S and Xu J 2010 Geometry- and size-dependence of electrical properties of metal contacts on semiconducting nanowires *J. Appl. Phys.* **108** 094308

[39] Gutsche C, Regolin I, Blekker K, Lysov A, Prost W and Tegude F J 2009 Controllable p -type doping of GaAs nanowires during vapor-liquid-solid growth *J. Appl. Phys.* **105**

[40] Stareev G 1993 Formation of extremely low resistance Ti/Pt/Au ohmic contacts to p -GaAs *Appl. Phys. Lett.* **62** 2801–3

[41] Küpers H, Lewis R B, Tahraoui A, Matalla M, Krüger O, Bastiman F, Riechert H and Geelhaar L 2018 Diameter evolution of selective area grown Ga-assisted GaAs nanowires *Nano Res.* **11** 2885–93

[42] Xu J, Towe E, Yuan Q and Hull R 1999 Beryllium doping and silicon amphotericity in (110) GaAs-based heterostructures: structural and optical properties *J. Cryst. Growth* **196** 26–32

[43] Ivanov S V, Kop'ev P S and Ledentsov N N 1991 Interplay of beryllium segregation and diffusion in heavily doped GaAs and AlGaAs grown by molecular beam epitaxy (thermodynamic analysis) *J. Cryst. Growth* **108** 661–9

[44] Pao Y C, Franklin J and Harris J S 1989 Influence of As4/Ga flux ratio on Be incorporation in heavily doped GaAs grown by molecular beam epitaxy *J. Cryst. Growth* **95** 301–4

Be-dopant gradients in self-catalyzed GaAs nanowires

Supplementary Data

Marcelo Rizzo Piton[1,2], Eero Koivusalo[2], Teemu Hakkarainen[2], Helder V. A. Galeti[3], Ariano D. Rodrigues[1], Soile Talmila[2], Sergio Souto[4], Donald Lupo[5], Yara Galvao Gobato[1,6] and Mircea Guina[2]

[1] *Physics Department, Federal University of São Carlos, São Carlos-SP, Brazil*

[2] *Optoelectronics Research Centre, Physics Unit, Tampere University, Tampere, Finland*

[3] *Electrical Engineering Department, Federal University of São Carlos, São Carlos-SP, Brazil*

[4] *FZEA/ZAB, University of São Paulo, Pirassununga-SP, Brazil*

[5] *Electronics and Communications Engineering, Tampere University, Tampere, Finland*

[6] *High Field Magnetic Laboratory, Radboud University, The Netherlands*

E-mail: marcelo.rizzopiton@tuni.fi

1. Nanowire-droplet contact angle statistics

Figure S6 shows the post growth Ga droplet contact angle statistics analysis of undoped, Be1 and Be2 NWs. The contact angles were measured from SEM images of the lateral view of 50-70 NWs from each sample. All the SEM images were obtained using the same electron acceleration voltage, working distance and magnification. The NWs were oriented in such way that the (110) facets were facing towards the in lens detector of the SEM. The mean values of contact angles and the standard deviations for undoped, Be1, and Be2 NWs are 127.8°±5.3°, 123.5°±4.6° and 126.4°±6.2° respectively.

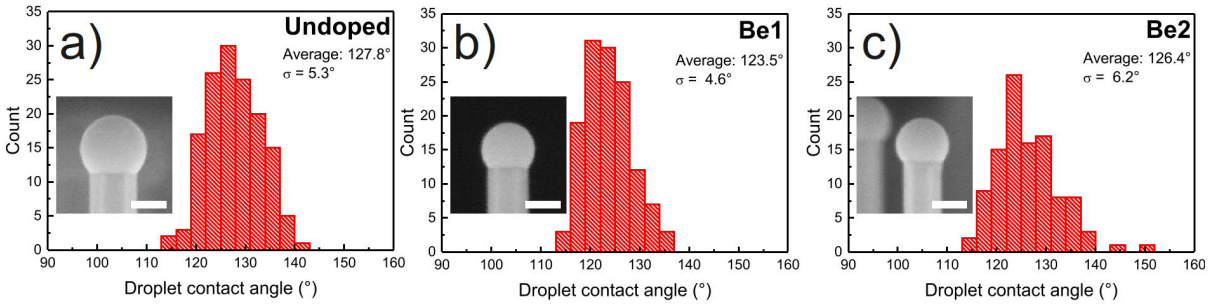

Figure S9: Droplet contact angle statistics of (a) undoped, (b) Be1 and (c) Be2 NWs. The insets show SEM images of representative NWs from each sample and the scale bars correspond to 100 nm.

2. Transmission Electron Microscopy

Figure S1 shows the selected area electron diffraction patterns (SAED) from the same position from of the HR-TEM images of undoped, Be1 and Be2 NWs in figure 1 of the main text. The SAED in figures S1(d), S1(h) and S1(l) show the high disorder of the bottom region of undoped, Be1 and Be2 NW respectively. The SAED of the center and tip regions of Be1 and Be2 NWs further confirm the lower density of twinned ZB GaAs in comparison to the undoped reference NW.

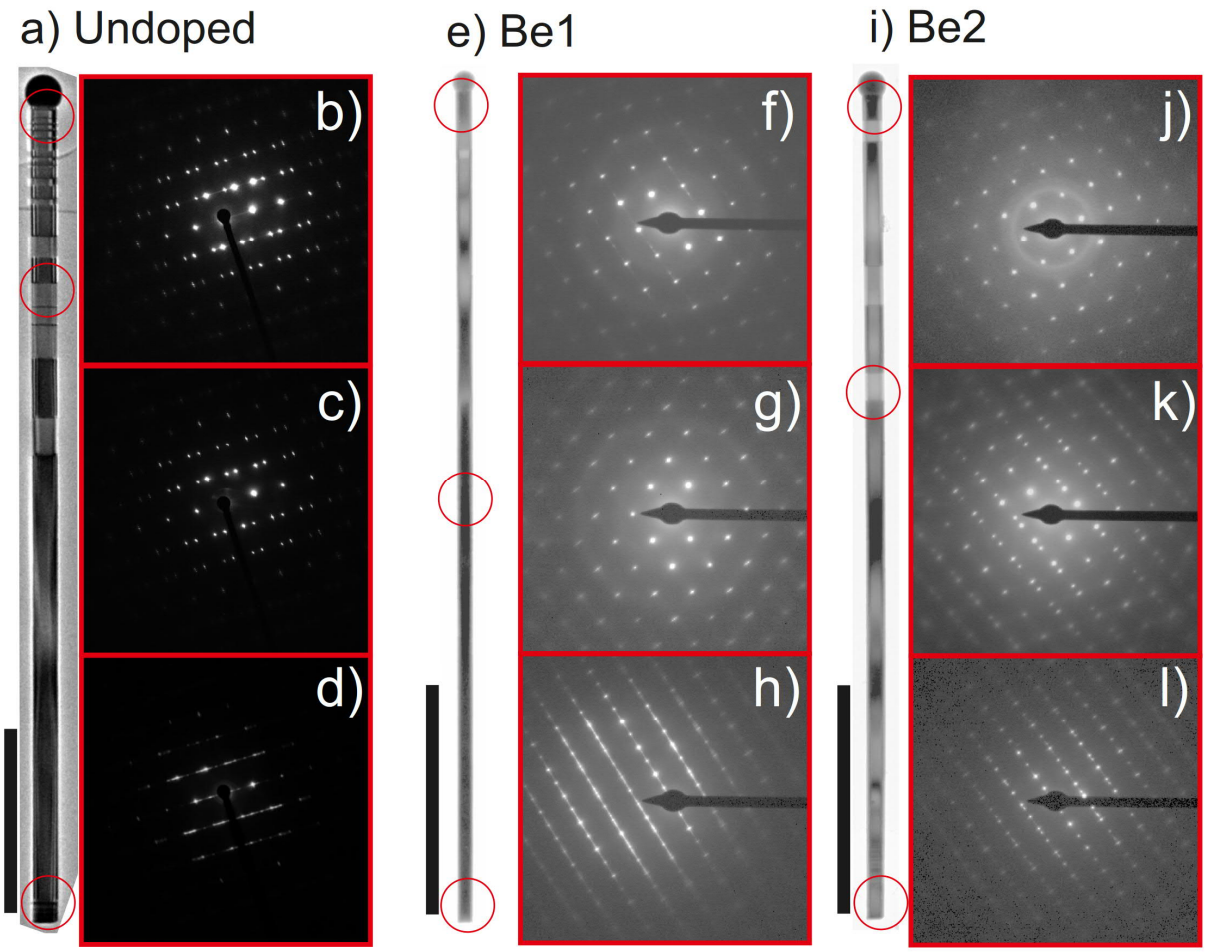

Figure S10: Low magnification HR-TEM images and SAED patterns of (a)-(d) undoped, (e)-(h) Be1 and (i)-(l) Be2 NWs. The red circles in (a), (e) and (i) indicate the position in the NW from where the SAED patterns in (b)-(d), (f)-(h) and (j)-(l) were obtained.

3. Raman spectroscopy

Figure S2 shows additional Raman data of similar Be-doped NWs. The SEM images on the right side of the spectra indicate the axial position of each NW from where the spectra were measured. The plasma frequency and damping constant obtained from the fit of the CPPM peak of each position in figure S2 were used to calculate the carrier concentrations and hole mobilities presented in figures 4(a) and 4(b) respectively.

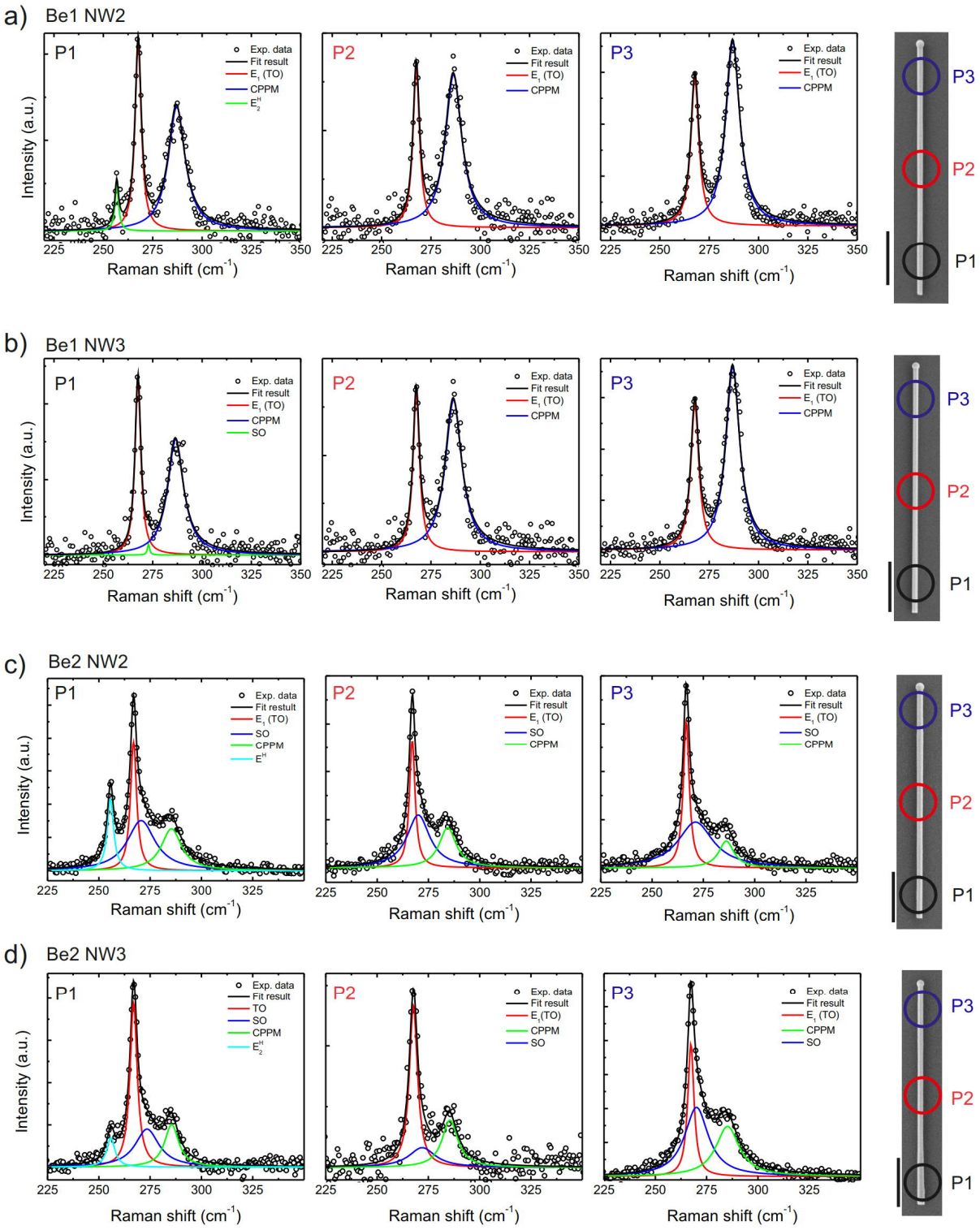

Figure S11: Raman spectra from three different axial positions of Be-doped NWs. (a) Be1 NW2, (b) Be1 NW3, (c) Be2 NW2 and (d) Be2 NW3. The spectra P1, P2, and P3 were collected from the regions indicated in the SEM pictures of the right sides of (a)-(d). The scale bars in the SEM pictures are 1 μm.

4. Transport properties

Figures S3 and S4 show additional IV and SEM data from devices with four evenly spaced contacts for NW samples Be1 and Be2, respectively. The IVs from Be1 NW2 and NW3 in figures S3(a) and S3(e) exhibit similar trend to the data presented in figure 5: asymmetric IV and different current values in different positions along the NWs. This behavior is associated to an increase in the values of the Schottky barrier heights in the metal-semiconductor contacts from bottom (AB channels) to tip (CD channels) of the NWs. Figures S4(a) and S4(e) show IV for Be2 NW2 and NW3 respectively. For these devices, the resistivity of the AB, BC, and CD channels were obtained from equation (5) and presented in figure 8.

As was discussed in Section 3.3, the Ga droplets were removed from some of the NWs during the contact fabrication process. The bottom and tip ends of the NWs in the devices shown in figures S3(b), S3(f), S4(b) and S4(f) were identified by the off-cut shape formed at the bottom end of the NWs, which was a consistent characteristic of the undoped and Be-doped NWs. This characteristic feature was observed in the TEM micrographs as well as in the SEM images of NWs used for Raman spectroscopy. Higher magnification SEM of the bottom region of the NWs are shown in figures S3(c), S3(g), S4(c), S4(g) and the tip region in figures S3(d), S3(h), S4(d) and S4(h). This trend in the NWs allowed us to identify with confidence the bottom and tip ends of the NWs, thus corroborating the results indicating different Be-dopant incorporation mechanisms discussed in the main text.

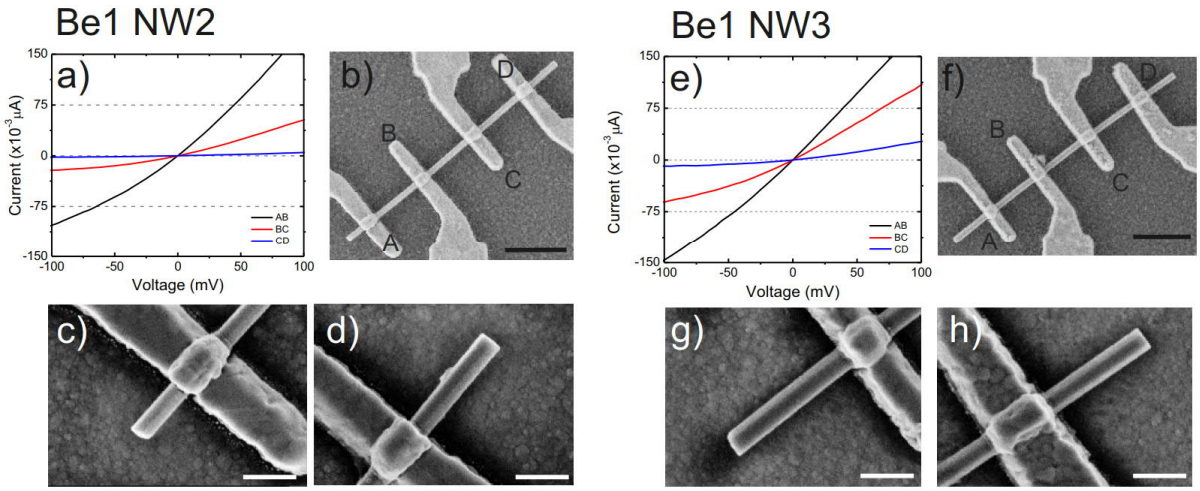

Figure S12: IV from Be1 NW2 (a) and NW3 (e) and the corresponding SEM images from the measured devices in (b) and (f). The A contact is close to the bottom and D contact close to the tip of the NW. The higher magnification SEM images of the NW ends were used to identify the bottom region of the NWs in (c),(g) and the tip region in (d) and (h). The scale bars are 1 µm in (b) and (f) and 250 nm in (c), (d), (g) and (h).

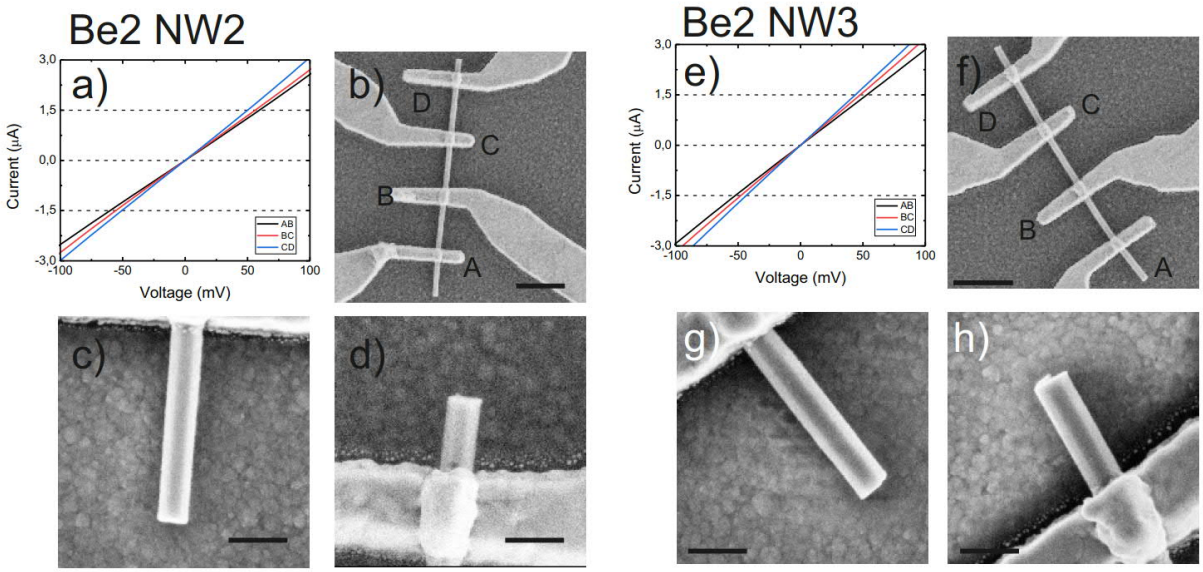

Figure S13: IV from Be2 NW2 (a) and NW3 (e) and the corresponding SEM images from the measured devices in (b) and (f). The A contact is close to the bottom and D contact close to the tip of the NW. The higher magnification SEM images of the NW ends were used to identify the bottom region of the NWs in (c),(g) and the tip region in (d) and (h). The scale bars are 1 µm in (b) and (f) and 250 nm in (c), (d), (g) and (h).

Since the off-cut at the bottom end of Be2 NW2 in figure S4(c) is not as evident as for the other NWs presented in figures S3 and S4, we show additional SEM images of Be2 NW2 from different perspectives in order to further confirm the bottom and top ends of the NW. Figures S5(a)-(d) show 30° tilted SEM pictures from a perspective perpendicular to the NW axis, obtained by properly aligning the NW in respect to the SEM detector and tilting the sample holder. From this perspective, we are able to identify the off-cut in figures S5(a) and (b) from the A contact in figure S4(b), which was ascribed to the bottom end of the NW. In contrast, figures S5(c) and (d) from D contact exhibit a flat surface at the end of the NW with residues of the Ga droplet, similar to observed in figure S4(h) from Be2 NW3, giving further confirmation that it was correctly ascribed to the top end of the NW. Figures S5(e)-(g) show additional SEM images of the bottom end (A contact), obtained by aligning the NW in a 45° in relation to the SEM detector and tilting the sample holder by 30°. The evidenced off-cut in figure S5(g) gives the necessary confirmation that the contact A indeed corresponds to the bottom end of the NW.

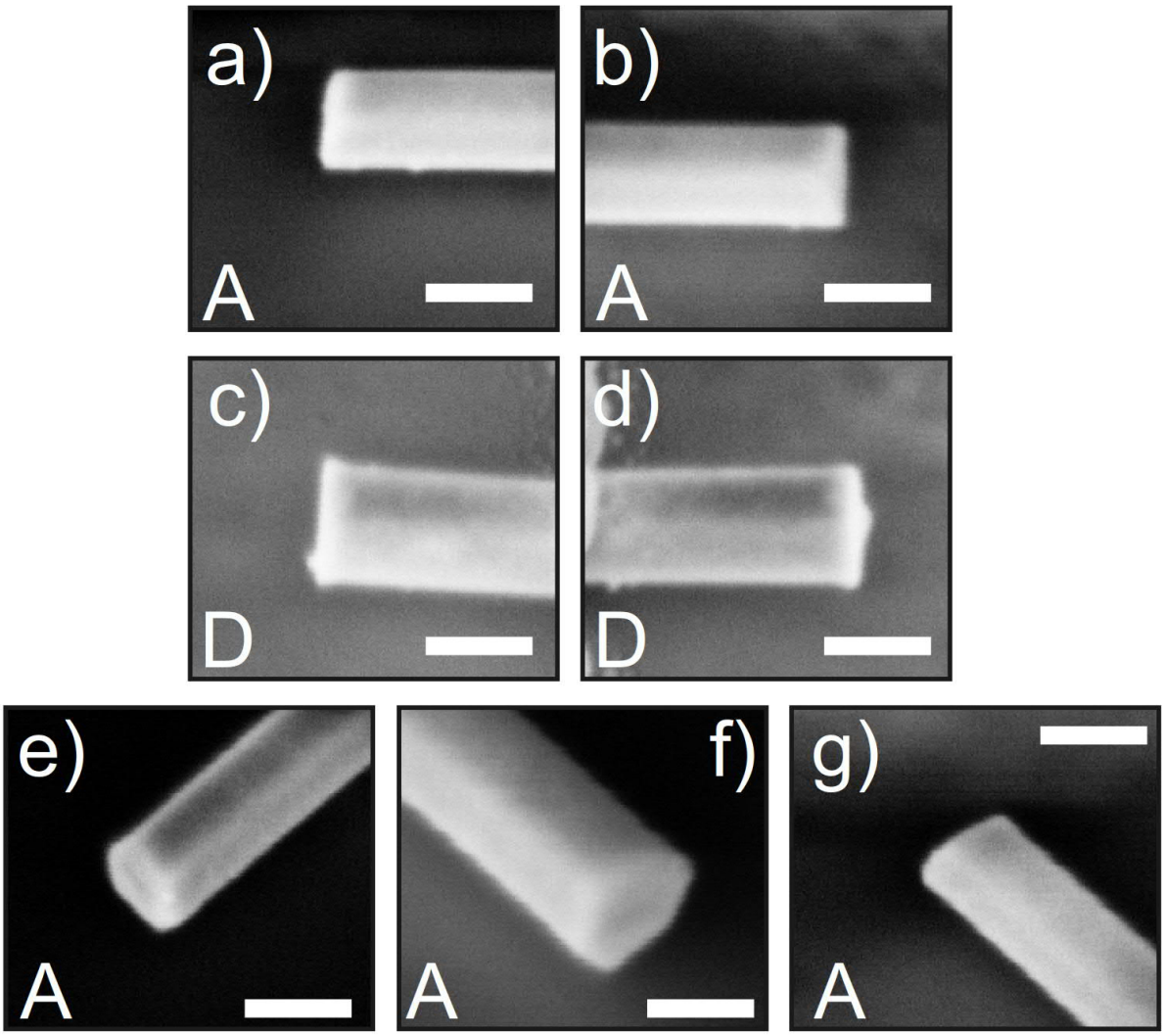

Figure S14: High magnification SEM images of NW end morphologies close to the A and D contacts of Be2 NW2 in figure S3 (a)-(d). The images were obtained from different perspectives by properly aligning the NW axis in respect to the SEM detector and tilting the sample holder by 30°. A perspective perpendicular to the NW axis is shown for the bottom region (A contact) in (a) and (b) and for the tip region (D contact) in (c) and (d). Additional perspectives on the A contact obtained by aligning the NW in a 45° angle in relation to the SEM detector and tilting the sample holder stage by 30° are shown in (e)-(g). The scale bars correspond to 100 nm.